Revista Mexicana de Astronomía y Astrofísica, **41**, 371–382 (2005)

FABRY-PEROT OBSERVATIONS OF HH 1/2[1]

A. Riera,[2,3] A. C. Raga,[4] B. Reipurth,[5] Ph. Amram,[6] J. Boulesteix,[6] and O. Toledano[7]

Received 2004 December 15; accepted 2005 April 1

RESUMEN

Presentamos nuevas observaciones Fabry-Perot del sistema HH1/2 en la línea de Hα. Se han obtenidos los perfiles de las líneas, y los mapas de velocidad radial y de dispersión de velocidades a partir de los canales de velocidad de los objetos HH 1 y HH 2. La distribución espacial de la velocidad radial de ambos objetos (HH 1, HH 2) presenta material desplazado al rojo hacia la fuente, y material desplazado al azul alejándose de la fuente. Un modelo que contempla la presencia de emisión directa+dispersada con tres condensaciones emisoras reproduce cualitativamente la distribución espacial de la velocidad radial y de la dispersión de velocidades de HH 2.

ABSTRACT

We present new Hα Fabry-Perot observations of the HH 1/2 system. Line profiles, barycenter radial velocity maps and dispersion maps are derived from the channel maps of HH 1 and HH 2. The radial velocity barycenter maps of both HH 1 and HH 2 show a general trend of "red-shifted upstream/blue-shifted downstream" pattern. A "direct+scattered" component model for three emitting condensations is qualitatively successful at reproducing the general features of the barycenter and the velocity dispersion of HH 2.

Key Words: **ISM: HERBIG-HARO OBJECTS — ISM: INDIVIDUAL (HH 1, HH 2) — ISM: JETS AND OUTFLOWS — ISM: KINEMATICS AND DYNAMICS**

1. INTRODUCTION

The HH 1/2 system is one of the brightest HH objects in the sky, and among the best studied. Since its discovery by Herbig (1951) and Haro (1952), the HH 1/2 system has been the subject of numerous studies in various wavelength ranges (e.g., radio: Rodríguez et al. 2000; infrared: Noriega-Crespo et al. 1997; UV: Böhm et al. 1987; X-rays: Pravdo et al. 2001).

The HH 1/2 system displays two bright groups of condensations in a bipolar flow, moving away from the central source, as shown by the measured proper motions (Herbig & Jones 1981; Noriega-Crespo et al. 1997; Eislöffel, Mundt, & Böhm 1994; Bally et al. 2002). The outflow emanates from a highly embedded source first detected at radio wavelengths by Pravdo et al. (1985), which is a multiple-star system (Reipurth et al. 2000; Rodríguez et al. 2000). Strom et al. (1985) discovered a small optical jet pointing from the VLA 1 source towards HH 1, which has recently been the object of a detailed study at optical and IR wavelengths with the *HST* (Reipurth et al. 2000).

Spectroscopic studies show that HH 1 and 2 are high-excitation objects, (e.g., Brugel, Böhm, & Mannery 1981; Hartmann & Raymond 1984), and their low radial velocities (Böhm & Solf 1985; Solf et al. 1991; Böhm & Solf 1992) and high proper motions (Herbig & Jones 1981; Bally et al. 2002) indicate that the flow lies close to the plane of the sky. Also, most of the papers reporting variability in HH flows are concerned with the optical (Herbig 1973; Raga, Barnes, & Mateo 1990) and UV (Böhm, Noriega-Crespo, & Solf 1993) variability of the HH 1/2 system.

[1] Based on observations collected at the European Southern Observatory, La Silla, Chile.

[2] Departament de Física i Enginyeria Nuclear, Universitat Politècnica de Catalunya, Spain.

[3] Departament d'Astronomia i Meteorologia. Universitat de Barcelona, Spain

[4] Instituto de Ciencias Nucleares, Universidad Nacional Autónoma de México, México.

[5] Institute for Astronomy, University of Hawaii

[6] Observatoire Astronomique Marseille-Provence & Laboratoire d'Astrophysique de Marseille, France.

[7] Instituto de Astronomía, Universidad Nacional Autónoma de México, México.

HST observations of HH 1 and 2 (Schwartz et al. 1993; Hester, Stapelfeldt, & Scowen 1998; Bally et al. 2002) show that while HH 1 might correspond to a single (though fragmented) bow shock, HH 2 is much more complex. The characteristics of HH 1 have been successfully modeled in terms of bow shock models (Hartmann & Raymond 1984; Raga & Böhm 1985; Choe, Böhm, & Solf 1985), with time-dependent models (Raga & Böhm 1987; Raga et al. 1988) showing that the condensation structure could be the result of instabilities in the post-bow shock flow, and 3D analytic models showing that the side-to-side asymetry of HH 1 could be the result of an environmental density gradient (Henney 1996). Finally, the spectroscopic characteristics of the knots of HH 1 and the surrounding, more diffuse emission have been interpreted in terms of the presence of a direct component (i.e., the direct emission from the knots) and a scattered component (i.e., the light from the knots which is scattered by the dust in the surrounding environment) by Noriega-Crespo, Calvet, & Böhm (1991) and Henney, Raga, & Axon (1994).

The physical conditions are much more complex in HH 2, which cannot be explained as a simple bow shock. Different scenarios have been proposed to explain the physical properties of HH 2. Hartigan, Raymond, & Hartmann (1987) proposed that HH 2 is formed by individual bullets ejected from the source, and Raymond, Hartmann, & Hartigan (1988) computed the most detailed ever "3/2-D" bow shock model, applying it to the condensation HH 2A. Torrelles et al. (1992) observed cold, dense gas traced by NH_3 emission clumps near HH 2 and suggested that a clumpy medium is responsible for the appearance of HH 2 (also see Girart et al. 2002). Schwartz et al. (1993) suggested that HH 2 is the fragmentation of a bow shock due to thermal instabilities. The very complex, spatially resolved line profiles of the region around HH 2 (Böhm & Solf 1992) appear to defy a simple "direct+scattered component" interpretation such as has been proposed for the region around HH 1 (see above and Noriega-Crespo et al. 1991).

From a qualitative analysis of *HST* images of the HH 1/2 system, Hester et al. (1998) conclude that HH 2H (the brightest knot in HH 2) is likely to be the current location of the active working surface of the jet. The knot HH 2H shows strong UV emission, exhibits some of the largest proper motions observed in the system, and has brightened optically relative to the other knots during the 1990s. HH 2H is the only knot that is seen in X-rays (Pravdo et al. 2001) and at radio wavelengths (Rodríguez et al. 2000).

Given the extensive, previous work on the HH 1/2 system (which is partially discussed above), it is hard to make a new observational contribution, especially at optical wavelengths. In particular, the multi-long slit spectroscopic studies of HH 1 and 2 of Böhm and collaborators (Solf et al. 1991; Böhm & Solf 1992) and previous, single long-slit studies (Böhm & Solf 1985; Solf, Böhm, & Raga 1988) have provided high and low spectral resolution information covering all of the spectrum from the UV to the IR, as well as having substantial spatial coverage. It is clearly difficult to contribute more information, at least with ground based data without adaptive optics corrections.

With these limitations in mind, we present new Hα Fabry-Perot data of the HH 1/2 system. These data have angular and spectral resolutions comparable to the ones of the multi-long slit spectra of Solf et al. (1991) and Böhm & Solf (1992), but have a more complete spatial coverage (particularly in the region around HH 2, where the data of Böhm and Solf 1992 do not cover a substantial part of the emission). These data allow us to study the spatial distribution of the barycenter and the width of the Hα line in more detail than was possible with the previously published data. This new study allows us to re-evaluate the interpretation of the HH 1 and 2 emission as a combination of a direct and a scattered component.

The Fabry-Perot observations are described in § 2. We show the Hα velocity channel maps, the Hα radial velocity barycenter and velocity dispersion maps, and the Hα line profiles of HH 1 and HH 2 in §§ 3 and 4. In § 5, we interpret the observations of HH 2 in terms of a "direct+scattered" component model for three emitting condensations, and discuss its successes and failures in describing the radial velocity barycenter and velocity dispersion maps. Finally, we present our conclusions and discussion in § 6.

2. OBSERVATIONS

The observations were carried out at the European Southern Observatory 3.6 m telescope, on January 3, 1997. The Fabry-Perot instrument CIGALE [8] was used. It is composed of a focal reducer (bringing the original f/8 focal ratio of the Cassegrain focus to f/2), a scanning Fabry-Perot

[8] The instrument CIGALE (for CInématique des GALaxieEs) is a visiting instrument belonging to the Laboratoire d'Astrophysique de Marseille.

TABLE 1

JOURNAL OF FABRY-PEROT OBSERVATIONS

Observations	Telescope	ESO 3.6 m
	Equipment	CIGALE @ Cassegrain
	Date	1997, January, 3
	Seeing	$\sim$ 2-3″
Calibration	Neon Comparison light	λ6598.95 Å
Fabry–Perot	Interference Order	793 @ 6562.78 Å
	Free Spectral Range at Hα	380 km s^{-1}
	Finesse[a] at Hα	12.5
	Spectral resolution at Hα	9900[b]
Sampling	Number of Scanning Steps	32
	Integration Time per Channel	5 seconds
	Total Integration Time	3 hours
	Sampling Step	0.26 Å ($\sim$ 12 km s^{-1})
	Total Field	170″×170″ (256×256 px^2)
	Pixel Size	0.91″
Filter[c]	Central Wavelength	6562.5 Å
	Line Observed	Hα 6562.78 Å
	FWHM	8.8 Å
	Maximum transmission	0.64
Detector	IPCS	Thompsom tube

[a]Mean *finesse* through the field of view.

[b]For a signal to noise ratio of 5 at the sample step.

[c]Corrected for the observational conditions of temperature and beam.

and an Image Photon Counting System (IPCS). Table 1 contains the journal of observations. The Hα line has been isolated using a narrow interference filter. We have used a Fabry-Perot with an interference order of p=*793@Hα* (380 km s^{-1}) and a *finesse (F=12.5)*. The free spectral range was scanned through 32 channels. The exposure time per elementary channel was 5 seconds. The total exposure time was 3 hours. The IPCS, with a time sampling of 1/50 second and zero readout noise, makes it possible to scan the interferometer rapidly, avoiding sky transparency, air-mass and seeing variation problems during the exposures and thus has several advantages over a CCD for this application. Reductions of the data cubes were performed using the CIGALE software.

The data reduction procedure has been described in Amram et al. (1998, and references therein). Wavelength calibration was obtained by scanning the narrow Ne 6598.95 Å line under the same conditions as the observations. The data were deconvolved of the instrumental profile, which is shown in Figure 1.

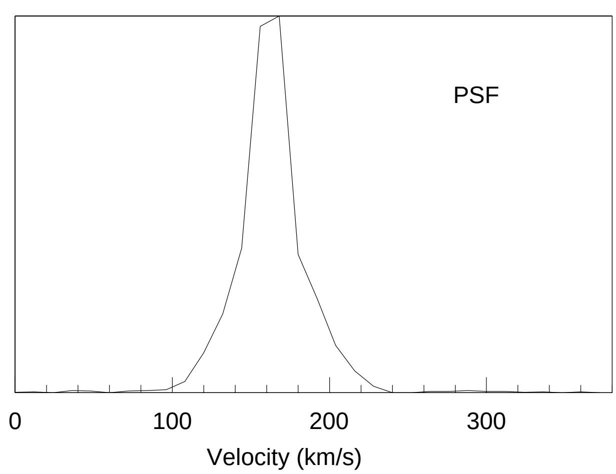

Fig. 1. The instrumental PSF obtained from the Neon line.

Velocities measured relative to the systemic velocity are very accurate, with an error of a fraction of a channel width ($<$ 3 km s^{-1}) over the whole field.

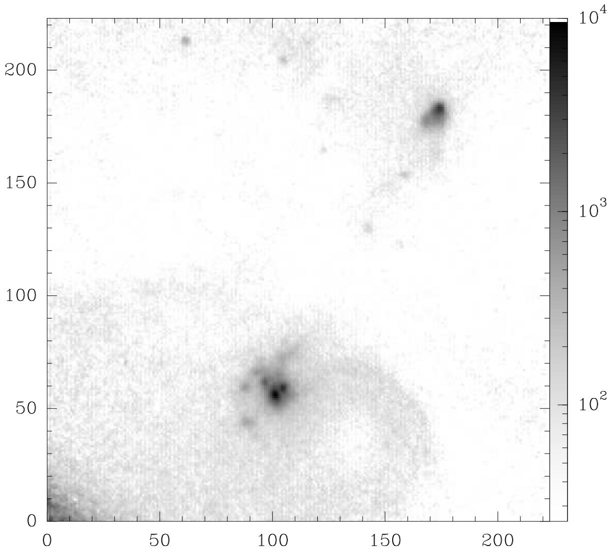

Fig. 2. The Hα image map of HH 1/2 region. The grey scale of the map (linear, in counts) is given by the bar. North is up and East to the left. The two axes are labeled in arcseconds.

The signal measured along the scanning sequence was separated into two parts: (1) an almost constant level produced by the continuum light in a narrow passband around the line(s) (referred hereafter as continuum map) and (2) a varying part produced by the line(s) (referred hereafter as the emission line map(s) or monochromatic map). The continuum level was taken to be the mean of the three faintest channels, to avoid channel noise effects. The line integrated flux map was obtained by integrating the monochromatic profile in each pixel. The velocity sampling was 12 km s^{-1}. Profiles were spatially binned to 3×3 or 5×5 pixels in the outer parts, in order to increase the signal-to-noise ratio. Night sky lines passing through the filters were subtracted by determining the level of emission from extended regions away from the HH object (Laval et al. 1987).

3. Hα CHANNEL MAPS

Figure 2 shows the integrated intensity map constructed by summing the Hα line over its wavelength extent in the data cube. In this map, one can clearly see the condensations of HH 1 (to the NW) and HH 2 (to the SE). In the following two subsections, we describe the velocity channel maps for the regions around HH 1 and 2.

3.1. *HH 1*

Figure 3 shows the velocity channel maps of HH 1. In several of the velocity channel maps, we detect the condensation structure that has been previously observed in this object.

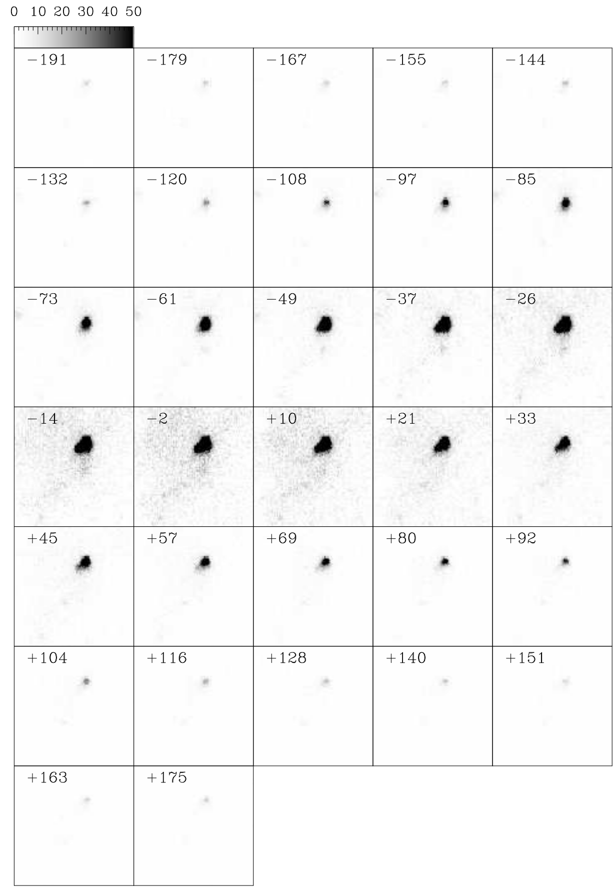

Fig. 3. Hα velocity channel maps corresponding to various radial velocities obtained from the Fabry-Perot data of HH 1. Labels correspond to the central heliocentric radial velocity of each channel (in km s^{-1}). The maps are shown with a linear greyscale given by the bar (in counts).

In the integrated Hα image (see Figure 4) we have identified some of the knots of HH 1. HH 1F is the brightest condensation. From this condensation, two wings extend towards the source. In the East wing, there are few condensations (labeled A, D, and C by Solf et al. 1991), which are not spatially resolved in our Fabry-Perot data, and have been labeled as A in Fig. 4. At low levels, we observe an elongated structure corresponding to the faint western edge of HH 1 (labeled G-H in Fig. 4).

For HH 1F, we detect emission ranging from $v_r \approx -180$ to $+170$ km s^{-1} (see Fig. 3). The surface brightness of knot 1F grows with increasig radial velocities, reaching a maximum at $v_r \approx -4$ km s^{-1}, and decreasing for larger radial velocities. The knot HH 1A is detected from -63 to $+100$ km s^{-1} heliocentric radial velocities, and shows a brightness maximum at $+8$ km s^{-1}.

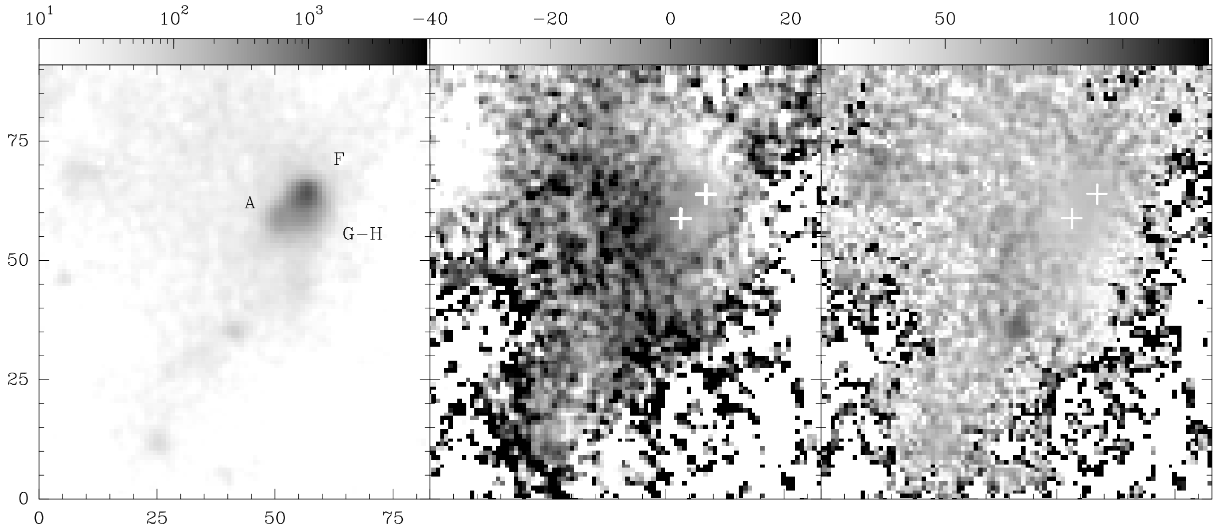

Fig. 4. Left panel: Hα map of HH 1. The observed knots are identified following the nomenclature of Herbig & Jones (1981) and Eislöffel et al. (1994). The greyscale of the maps is given by the bar (in counts). Central panel: Hα barycenter radial velocity map obtained from the position-velocity cube. The greyscale (linear, in km s^{-1}) is given by the bar. Right panel: Hα line dispersion map obtained from the position-velocity cube. The greyscale (linear, in km s^{-1}) is given by the bar. The crosses indicate the positions of condensations F and A. The two axes are labeled in arcseconds.

From the line profiles at each pixel, we have computed the velocity of the barycenter and the dispersion. In order to increase the signal-to-noise ratio, we have carried out a 2×2 spatial binning of the channel maps. The resulting maps are shown in Fig. 4. The brighter condensations of HH 1 have barycenter velocities ≈ -12 km s^{-1} and -8 km s^{-1} for the knots HH 1F and HH 1A, respectively. The barycenter radial velocities change across HH 1, from -30 km s^{-1} at $7''$ beyond knot HH 1F to 20 km s^{-1} at $6.5''$ from knot HH 1F towards the source. This "upstream red/downstream blue shifted" effect has been observed previously (in long slit spectra), and interpreted as evidence for a scattered light component, which reflects the motion of HH 1 with respect to the dusty surrounding environment (Noriega-Crespo et al. 1991; Henney et al. 1994).

3.2. *HH 2*

Figure 5 shows the velocity channel maps of the region around HH 2. As HH 2 is brighter than HH 1, we have not binned the data spatially (as we have done for HH 1, see § 3.1). In Figure 6, we present the Hα intensity map of HH 2, where we have identified the observed knots. We should note that knots B, C, D, and I are not spatially resolved.

We detect Hα emission in all channels, i.e., for heliocentric radial velocities ranging from -190 to $+180$ km s^{-1} (see Fig. 5). Condensations 2H and 2A are detected in all of the channel maps. At radial velocities larger than $+59$ km s^{-1}, the Hα emission of HH 2 is dominated by condensation 2H.

The surface brightness of knot 2H grows with increasing radial velocities, reaching a maximum emission level in the -47 km s^{-1} channel map. It then decreases, reaching a minimum at $+1$ km s^{-1}, and increases again reaching a second maximum at $+61$ km s^{-1}. For larger velocities the surface brightness decreases.

Knot 2A is observed as a bright condensation in the channel maps corresponding to radial velocities ranging from -130 to $+85$ km s^{-1}. The surface brightness of HH 2A also grows with increasing radial velocity, reaching a maximum emission level in the range from -47 to -35 km s^{-1}.

At $v_r \approx -97$ km s^{-1}, condensation 2G is observed as a faint knot at $\sim 7''$ from knot HH 2H. The surface brightness of 2G increases with increasing radial velocities, reaching a maximum at -35 km s^{-1} and decreasing for larger radial velocities. Condensation G is not observed in the channel maps corresponding to radial velocities larger than $+71$ km s^{-1}.

The faint knots HH 2L, E, K, T, and R (identified in Fig. 6) were observed in the Hα channel maps with radial velocities from ~ -50 up to $+80$ km s^{-1}. The surface brightness of these condensations increases for radial velocities > -50 km s^{-1}, reaching a maximum (at velocities from -11 to $+25$ km s^{-1}) and then decreases.

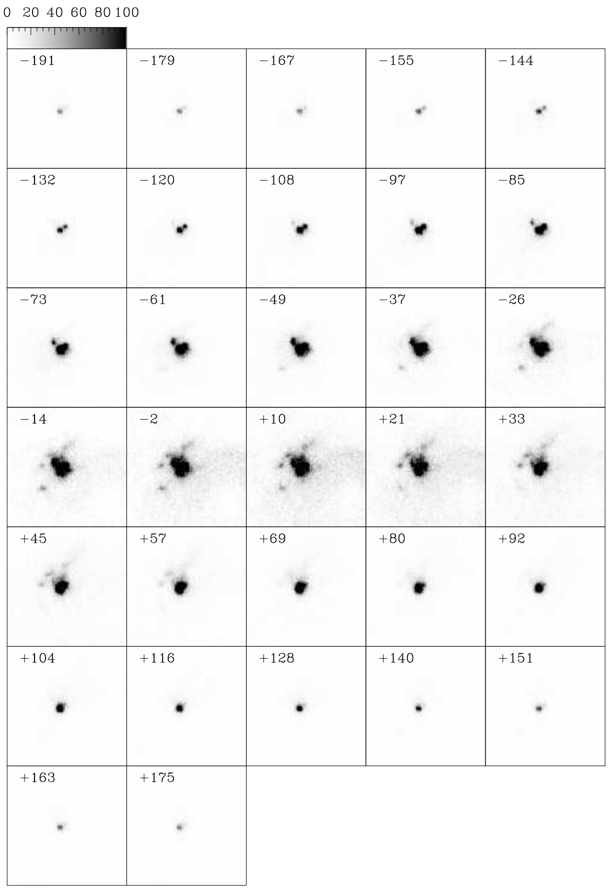

Fig. 5. Hα velocity channel maps corresponding to various radial velocities obtained from the Fabry-Perot data of HH 2. Labels correspond to the central heliocentric radial velocity of each channel (in km s^{-1}).

The map with the velocities corresponding to the barycenter of the line profiles (central frame of Fig. 6) shows a complex structure of intermingling "tongues" of red- and blue-shifted emission. The velocity dispersion map (right, Fig. 6) shows a maximum of $\sim$ 100 km s^{-1} in the region of knots A and H (the two brightest knots of HH 2), and lower values of $\sim$ 60 km s^{-1} in the rest of HH 2. In their long-slit spectroscopic data, Böhm & Solf (1992) detected the rather complex radial velocity structure as well as the velocity dispersion maximum in the region of knots A and H. These authors argued that this structure did not appear to agree with the results expected from a "direct+scattered emission" model. We re-analyze this issue in § 5.

4. EMISSION LINE PROFILES

In order to have a better understanding of the kinematics of HH 1 and 2, we have obtained Hα emission line profiles for each condensation of HH 1 and HH 2. The results are presented as relative intensity (in counts) versus heliocentric radial velocity.

4.1. *HH 1*

In Figure 7, we present the Hα emission line profiles of condensations HH 1F, A, and G-H.

Knot 1F shows a wide, single-peaked emission line profile, which can be fitted by a single Gaussian profile centered at $v_r \sim -11$ km s^{-1} and a FWHM of 104 km s^{-1}. These values are in agreement with the results obtained from the velocity data cube and obtained by other authors (see § 3.1).

The Hα emission line profiles of HH 1A and HH 1G-H cannot be fitted by a single Gaussian profile. The Hα profile of HH 1A is a more or less symmetric profile (shown in Fig. 7). This profile is best fitted by three Gaussian profiles: the brightest central component at a heliocentric radial velocity of -3 km s^{-1} and FWHM of 70 km s^{-1}, and two components (blue + red) of lower intensity at radial velocities of -93 and $+59$ km s^{-1}. The Hα line profile of HH 1 G-H shows an asymmetric profile with a blueward excess. This profile is best fitted by three Gaussian profiles at heliocentric radial velocities of -45, -1, and $+41$ km s^{-1}. The Gaussian component at -45 km s^{-1} corresponds to the blue 'bump" seen in the Hα line profile of HH 1G-H (see Fig. 7), while the brightest component is centered at -1 km s^{-1}.

The central radial velocities measured by Böhm & Solf (1985) for HH 1 are similar to the values obtained by us from the Fabry-Perot data. However, there are some differences regarding the FWHM of the Hα emission lines measured in both studies. Solf et al. (1991) found larger line widths in HH 1G than in HH 1A (by $\sim$ 30%). A difference which is not seen in the Fabry-Perot data, where we may not be spatially resolving the A, C and G, H condensations.

4.2. *HH 2*

In Figure 8, we present the Hα emission profiles of the knots of HH 2. Some of the knots show asymmetric, single-peaked profiles (knots L, E, B, C, K, T, and R). The brightest knot of HH 2 -knot H- shows a double-peaked emission line profile. The other knots (A, I, D, and G) show broad emission line profiles.

The emission line profiles of knots L and E show a single, central peak and a blueward wing, which are appropriately fitted by two Gaussian profiles. The central bright component is centered at -1 and $+20$ km s^{-1} for knots L and E, respectively. The emission line profiles of both knots (HH 2L and E) required a lower intensity Gaussian component at -54 km s^{-1}.

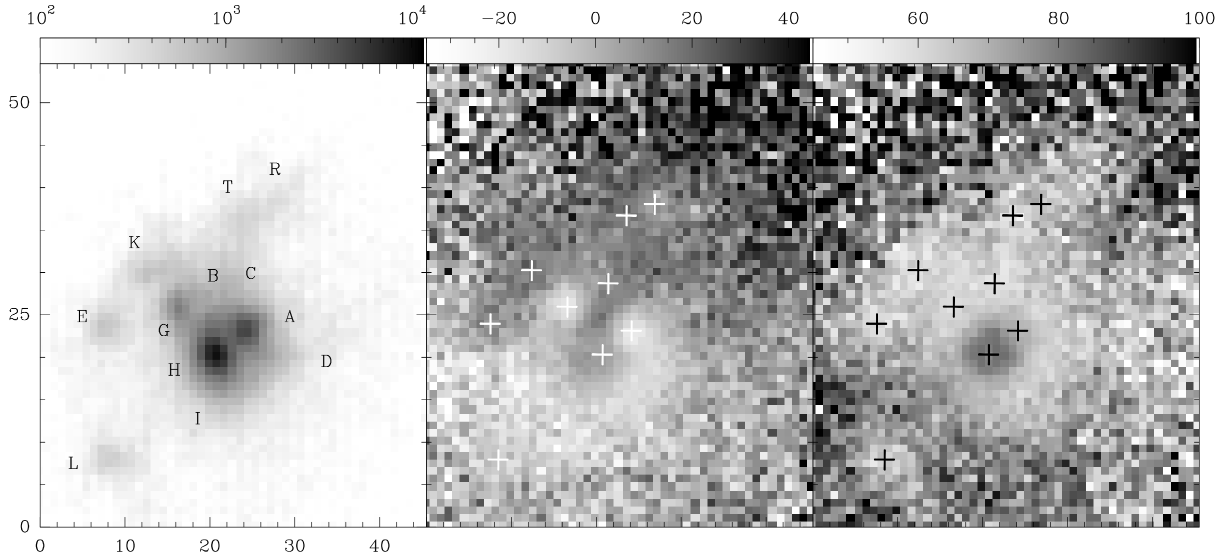

Fig. 6. As Fig. 4 but for HH 2. The crosses indicate the position of the knots of HH 2, with the exception of knots B, D, and I, which were not spatially resolved.

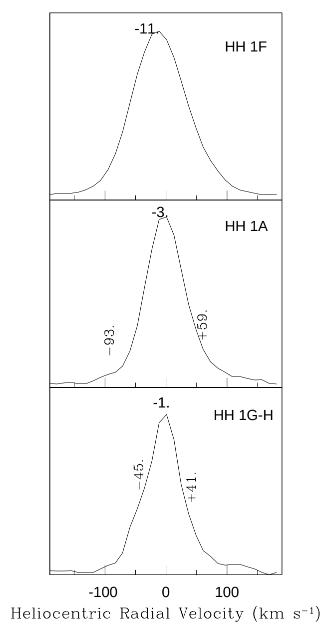

Fig. 7. Emission line profiles of HH1 F (top), A (center) G-H (bottom) obtained by integrating the emission over the knots. The relative intensities (in counts) as a function of the heliocentric radial velocities (in km s^{-1}) are presented. The heliocentric radial velocities of the Gaussian components are also indicated (see the text).

Knots E and L show narrow emission line profiles (as previously reported by Böhm & Solf 1992).

The Hα emission line profile of knot HH 2T can be fitted by a single Gaussian centered at +14 km s^{-1}. For knots K, R, G, B, and C, three Gaussian components are required to fit the observed Hα emission line profile. The brightest component is centered at: +15 (knot K), +9 (R), +5 (G), −4 (B) and +12 (C) km s^{-1}. The observed blueward excess can be fitted by another Gaussian component, centered from −60 to −52 km s^{-1}. An additional redward Gaussian component was needed to reproduce the observed emission line profiles for this group of knots. These red components are centered at radial velocities ranging from +63 to +72 km s^{-1}.

The HH 2A knot shows a broad emission line profile which can be fitted by a single Gaussian component centered at −5 km s^{-1} with a FWHM of 160 km s^{-1}. Böhm & Solf (1992) detected the highest velocity dispersion of HH 2 at knot 2A, with a FWHM larger than 160 km s^{-1}, which is in agreement with the values we obtain from the Fabry-Perot data.

The bright knot HH 2H shows a double-peaked emission line profile which can be fitted by two Gaussian components at −52 and + 58 km s^{-1}. The presence of a double-peaked emission line profile at knot HH 2H has not been reported before (see, e.g., Böhm & Solf 1992).

Finally, knots HH2 I and D show broad emission line profiles. We should note that, at the limited angular resolution of our observations, these knots overlap with the bright knots H and A.

In Figure 9, we present the Hα emission line profiles for the HH 2A knot. In this figure, the relative intensity (in counts) is plotted for each pixel (with a spatial scale of $0''.91 \times 0''.91$ per pixel) as a function of heliocentric radial velocity. The emission line pro-

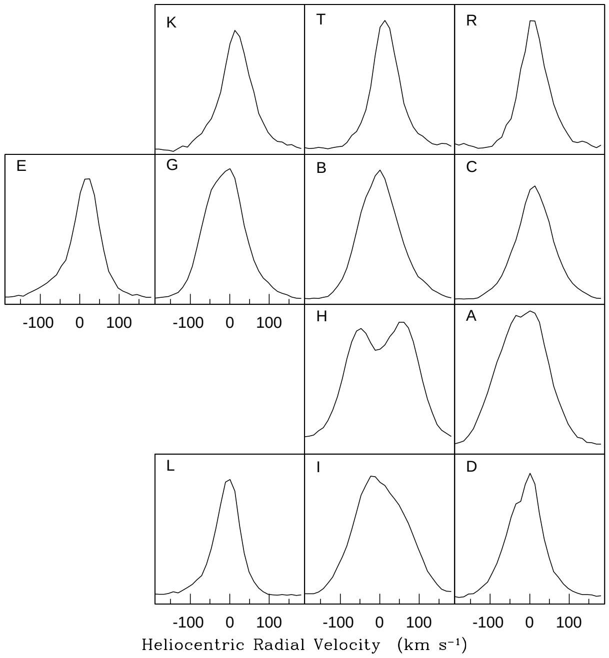

Fig. 8. Emission line profiles of several knots of HH 2 obtained by integrating the emission over the knots. The relative intensities (in counts) as a function of the heliocentric radial velocities (in km s^{-1}) are presented.

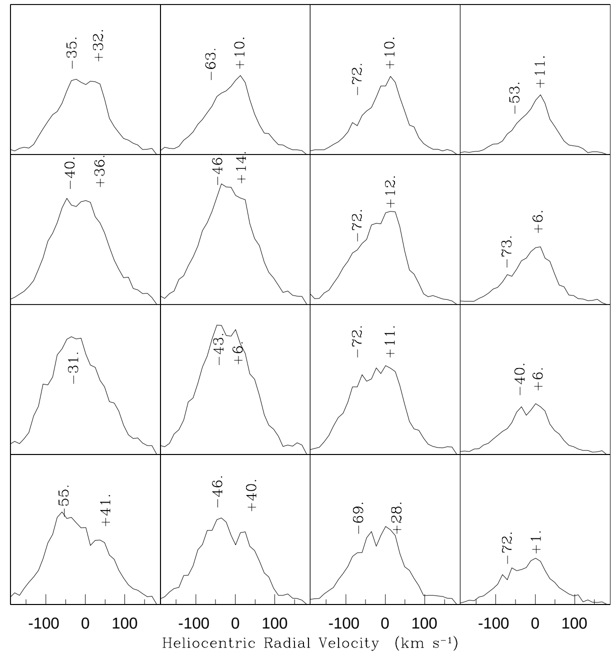

Fig. 9. Hα emission line profiles of HH 2A. The emission line profiles of each pixel (corresponding to 0.91$''$ $\times$ 0.91$''$) are plotted as relative intensity (in counts) vs. heliocentric radial velocity. The spatial field presented in this figure is 3.64$''$ $\times$ 3.64$''$ and corresponds to the region of knot HH 2A. The observed emission line profiles were fitted with two Gaussian components. The central velocities of these Gaussian profiles are also indicated (in km s^{-1}). North is up and East to the left.

files presented in this figure show broad and asymmetric profiles. The FWZI of the Hα emission line profiles are $\sim$ 300 km s^{-1}. The emission line profiles corresponding to the pixels at the top of Fig. 9 show asymmetric profiles with a blue-shifted excess, while some of the pixels at the bottom of this plot show line profiles with a red-shifted excess.

In Figure 10, we present the Hα emission line profiles for the HH 2H knot. The central profile corresponds to the brightest region of HH 2H. The double peaked profiles have been fitted by two Gaussian profiles centered at the velocities indicated in Figure 10, which we refer to as the blue- and the red-shifted components, respectively. The FWHM of the Gaussian components range from 75 to 110 km s^{-1}.

Figure 10 illustrates the variation of the relative intensities of the blue and the red components from S to N across HH 2H. The red component is stronger than the blue component towards the South. In the central pixels, the strength of both components is comparable. Towards the North, the blue component is slightly stronger than the red component.

The quantitative variation of the blue- and red-radial velocities (derived by the Gaussian line fit) is presented in Fig. 10. The heliocentric radial velocity of the red component increases from the South to the North (from a value of $\sim$ +50 km s^{-1} up to a value $\sim$ +68 km s^{-1}), while the absolute value of the radial velocity of the blue-shifted component decreases from South to North (from a value of $\sim$ -62 km s^{-1} to $\sim$ -40 km s^{-1}).

5. THE "DIRECT+SCATTERED COMPONENT" MODEL

It has long been suggested that the emission line profiles of HH objects might be a combination of a "direct component" revealing the intrinsic properties of the knot emission and a "scattered component" with kinematical properties that reflect the motion of the knots with respect to the surrounding, dusty environment (Calvet et al. 1992). The main application for this model has been in the interpretation of the long-slit spectra of HH 1, which show blue-shifted line profiles in the region beyond condensation 1F. This feature has been modeled in some detail by Noriega-Crespo et al. (1991) and by Henney et al. (1994).

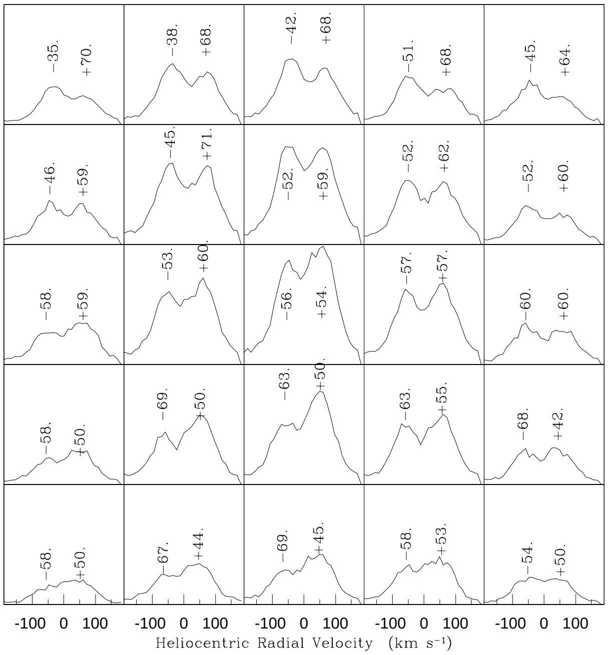

Fig. 10. Hα emission line profiles of HH 2H. The emission line profiles of each pixel (corresponding to 0.91″ × 0.91″) are plotted as relative intensity (in counts) vs. heliocentric radial velocity. The spatial field presented in this figure is of 4.55″ × 4.55″ and corresponds to the region of knot HH 2H. The observed emission line profiles were fitted with two Gaussian components. The central velocities of these Gaussian profiles are also indicated (in km s^{-1}). North is up and East to the left.

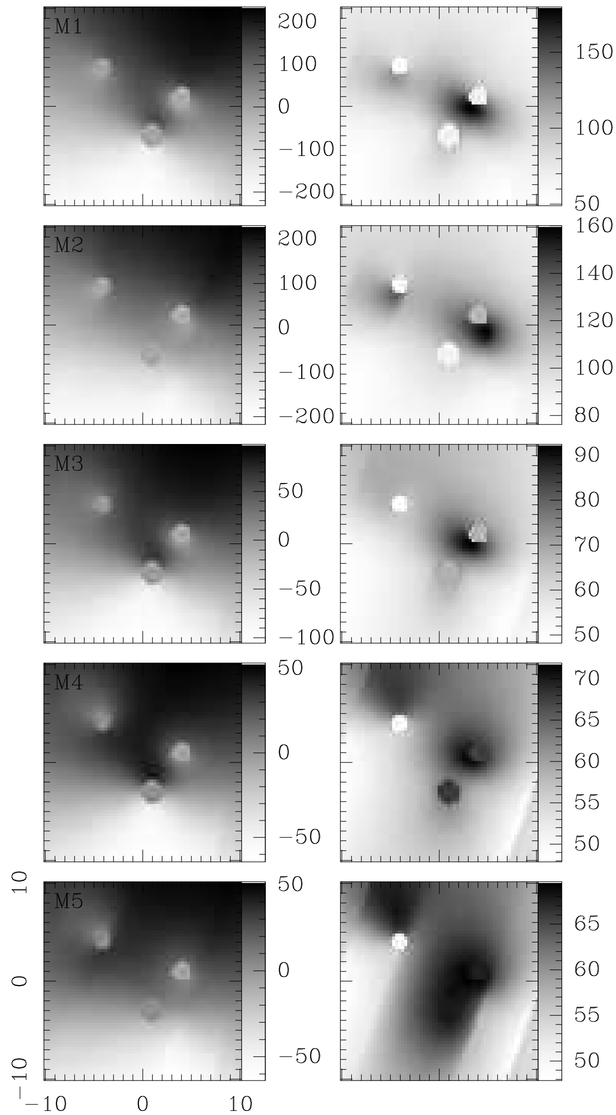

Fig. 11. Barycenter (left) and velocity dispersion (right) maps predicted from the five models described in the text (also see Tables 2 and 3). The two axes are labeled in arcseconds as offsets from a position in the middle of HH 2. The maps are shown with linear greyscales given in km s^{-1} by the bars to the right of each plot.

Our present observations basically confirm the fact that the line profiles of HH 1 appear to be the combination of a direct component (which peaks at condensation 1F) and a diffuse, scattered component. This scattered component is visible in the extended emission around HH 1, which is blue-shifted upstream of condensation 1F and red-shifted downstream of HH 1F (as can be seen in the central panel of Fig. 4). If one compares these results with the extensive theoretical study of Henney (1994), Henney et al. (1994) and Henney & Axon (1995), it is clear that the observations agree qualitatively well with the predictions from "direct+scattered component" models.

The situation is of course more complex in HH 2. In Figure 6, we see that there is a large scale structure of blue-shifted emission downstream and red-shifted emission upstream of HH 2, which is of course in qualitative agreement with what one would expect from the "direct+scattered component" model. However, the region around the three bright condensations H, A, and G shows a complex structure of interlacing "tongues" of red- and blue-shifted emission. It is not clear whether or not such structures could be explained in terms of the "direct+scattered component" interpretation.

In Fig. 6, we also see that the dispersion of the line shows a well defined maximum in the region of condensations H and A. Böhm & Solf (1992) have already commented on this feature, and have argued that it is difficult to interpret this line width maximum in terms of the "direct+scattered component" interpretation. This difficulty comes from the

TABLE 2

PARAMETERS FOR THE THREE EMITTING KNOTS USED IN THE MODELS

	H[a]	A[a]	G[a]
$v_{\rm RA}$ [km s^{-1}][b]	−73	−78	−82
$v_{\rm DEC}$ [km s^{-1}][b]	−272	−214	−141
v_r [km s^{-1}][c]	−52, 58	−5	5
$FWHM$ [km s^{-1}][c]	95	160	115
Δ(RA) [$''$][d]	1	4	−4
Δ(DEC) [$''$][d]	−3	1	4
$\Delta(z)$ [$''$][d]	0.5	−2	2
r_c [$''$][d]	1.2	1.0	0.8
relative intensity[c]	1.0	0.5	0.23

[a]The parameters have been chosen to approximate the properties of condensations HH 2H, A, and G.

[b]The proper motions have been taken from Eislöffel et al. (1994) and Bally et al. (2002).

[c]The radial velocities, FWHM and relative intensities of the emission of the knots have been taken from the central pixels of the corresponding condensations in our Fabry-Perot observations. The Hα profiles of knot H has been approximated with two Gaussians (of identical FWHM and intensities) centered at the two radial velocities given in the table.

[d]The positions of the knots are given as offsets from a position in the middle of HH 2. The chosen offsets $\Delta(z)$ along the line of sight are arbitrary. The radii of the knots have been estimated from Hα images of HH 2.

TABLE 3

PARAMETERS FOR THE 5 COMPUTED MODELS

Model	r_{in} [$''$][a]	r_{out} [$''$][a]	v_{env} [km s^{-1}][b]
M1	0	10	0
M2	5	10	0
M3	0	10	150
M4	0	10	200
M5	5	10	200

[a]Inner and outer radii of the cylindrical scattering envelope, which is aligned with the PA≈ 160° direction of the HH 1/2 outflow.

[b]Velocity of motion of the scattering envelope, directed along PA= 160°.

fact that models of a single emitting condensation in a scattering environment predict larger line widths away from the knot (see, e.g., Noriega-Crespo et al. 1991).

In order to evaluate in more detail whether or not a "direct+scattered component" interpretation is appropriate for HH 2, we have computed a series of 5 single scattering models. In these models, we consider 3 emitting condensations, with properties chosen to resemble the ones of knots HH 2 H, A, and G. The properties of the knots in the model are given in Table 2.

The knots in the model are spherical, and with a constant emission coefficient and intrinsic emission profile within the spheres. The diameters of the spheres have been chosen to resemble the sizes observed for the three corresponding knots in images of HH 2. The 3 knots have been given the relative (spatially integrated) positions and intensities obtained from our Hα image (see Figs. 2 and 6).

The intrinsic emission line profiles of the knots have been chosen to resemble the Hα profiles that we observe for the peaks of knots H, A, and G. We have modeled the intrinsic emission of knots A and G with a single Gaussian profile, and the emission of knot H with two Gaussians centered at different radial velocities (with the parameters given in Table 2). We should note that with our choice of intrinsic emission for knot H, the emission (of this knot) along the line of sight has two well separated Gaussian peaks, but these peaks merge into a single one when the knot is viewed along directions close to the plane of the sky.

We have then considered that these three knots are embedded in an envelope of dusty gas, which scatters the light from the three emitting knots. For carrying out the single scattering computation, we choose an envelope of cylindrical shape, with the axis of the cylinder approximately coinciding with the HH 1/2 outflow axis. The cylinder has a scattering optical depth of 0.1 across its diameter (in all models), an outer radius $r_{out} = 10''$ and we have considered cases in which there is a cylindrical hole in the scattering material of radius $r_{in} = 5''$ as well as cases in which the scattering material permeates the region in between the three emitting knots.

We have considered cases in which the scattering material is at rest, and cases in which the material is moving along the outflow axis with different velocities v_{env}. Finally, we have computed the models assuming a simple Henyey-Greenstein phase function for the scattering, with an asymmetry parameter $g = 0.7$. We then present 5 models (M1 through M5) with the parameter combinations listed in Table 3.

Figure 11 shows the barycenter and dispersion maps predicted from the 5 single scattering models carried out with the parameters described above (also see Tables 2 and 3). From this figure it is clear that all of the computed models resemble the observations of HH 2 (see Fig. 6) in a qualitative way. All of the models show barycenter maps with blue-shifted emission upstream and red-shifted emission downstream of the three bright knots (corresponding to knots H, A, and G of HH 2), and with a complex structure of interlacing "tongues" of emission with different radial velocities in the region in between the three knots.

In Fig. 11 we see that the velocity dispersion maps show a well defined peak in the region between the two brighter knots (which correspond to condensations HH 2H and A). This effect is due to the fact that in this region we see a superposition of the blue-shifted component of light scattered from knot A and the red-shifted component of light scattered from knot H. In this way, we see that it is indeed possible to interpret the line width maximum observed in the region of the condensations HH 2H and A (see Fig. 6 and Böhm & Solf 1992) in terms of a "direct+scattered component" model.

From Fig. 11, we see that while all of the models show qualitatively similar structures, the models in which the scattering environment is moving along the outflow axis have lower barycenter and velocity dispersion values. A comparison with the barycenter and dispersion values of HH 2 (see Fig. 6) indicates that the models with a non-stationary environment might be more appropriate for describing this object. This result suggests that we might be witnessing the entrainment of a dusty environment into the HH 1/2 outflow.

As can be seen from a comparison of the predictons from models M1 and M2, at least for some combinations of model parameters the assumptions of a "hollow" or "filled" medium produce very similar velocity barycenter and dispersion maps. On the other hand, model M5 (with a "hollow" medium) produces an extended high velocity dispersion region which is not observed in HH 2, and the predictions from model M4 (with identical parameters but with a "filled" medium) agree better with the observations. On the basis of these results, it is difficult to say whether or not the observations rule out the possibility of having a "hollow" medium.

6. CONCLUSIONS

We have presented new Hα Fabry-Perot observations of the HH 1/2 system. These data provide information similar to the one available from previous, long slit spectroscopy of this system (see, e.g., Solf et al. 1991 and Böhm & Solf 1992), but with a more complete spatial coverage.

In HH 1 (see Fig. 4) we see the 2D distribution of the diffuse red-shifted (upstream from HH 1F) and blue-shifted (downstream from 1F) emission, which has been interpreted in the past as the scattering of the light from HH 1 in the surrounding, dusty environment.

The Hα emission line profiles of the HH 1 knots show wide, asymmetric profiles with a blueward excess. The knots of HH 2 show single-peaked, broad emission line profiles, except knot 2H which shows a double-peaked emission line profile (see Fig. 8). Across knot 2H, the relative strength of the blue and the red components, and the velocities of the blue and red peaks change (along the N to S direction, as shown in Fig. 10). The presence of a double-peaked emission line at knot HH 2H has not been reported before. This might be the result of a time-variability of the line profile.

For HH 2 (see Fig. 6), we also see a general "red-shifted upstream/blue-shifted downstream" pattern for the radial velocity barycenter of the line profiles, with a complex interface between the red- and blue-shifted regions. The radial velocity dispersion shows a compact maximum in the region between condensations H and A, which had been detected before by Böhm & Solf (1992). From single scattering calculations in which we place three emitting knots with properties similar to the ones of the HH 2H, A and G condensations (see Fig. 11), we find that the models reproduce the main features of the barycenter and dispersion maps of HH 2. This is an interesting result, in that it shows that the interpretation previously suggested for modelling the spatially extended emission around HH 1 (Noriega-Crespo et al. 1991; Henney et al. 1994) also appears to be appropriate for HH 2.

Böhm & Solf (1992) mention that the bright condensations of HH 2 appear to have a spectrum with different excitation from the one of the extended emission in between the knots and around HH 2. They correctly argue that this difference in excitation appears to go against a "direct+scattered component" interpretation of HH 2. There might be ways to solve this discrepancy. For example, the brighter condensations could have a compact, high excitation emission region, surrounded by a somewhat more extended, lower excitation region, and then the scattered light would have an "in between" excitation (i.e., an excitation lower than the one of the compact, high excitation regions of the knots).

It is of course an open question whether such a possibility actually applies to HH 2, and our present observations (which are limited to the Hα line) do not contribute to possible solutions. A possible way to go forward on the problem of trying to reconcile the excitation of HH 2 with a "direct+scattered component" interpretation might be to attempt to model the high resolution HST images (in different emission lines) of HH 2 obtained by Hester et al. (1998). We leave an analysis of this possibility for a future paper.

We acknowledge an anonymous referee for her/his helpful comments. The work of ACR was supported by the CONACyT grants 36572-E and 41320 and the DGAPA (UNAM) grant IN 112602. The work of AR was supported by a grant from the Spanish Ministry of Science and Technology (AYA 2002-00205).

REFERENCES

Amram, P., Mendes de Oliveira, C., Boulesteix, J., & Balkowski C. 1998, A&A, 330, 881
Bally, J., Heathcote, S., Reipurth, B., Morse, J., Hartigan, P., & Schwartz, R. D. 2002, AJ, 123, 2627
Böhm, K. H., Bührke, Th., Raga, A. C., Brugel, E. W., Witt, A. N., & Mundt, R. 1987, ApJ, 316, 349
Böhm, K. H., Noriega-Crespo, A., & Solf, J. 1993, ApJ, 416, 647
Böhm, K. H., & Solf, J. 1985, ApJ, 294, 533
________. 1992, AJ, 104, 1193
Brugel, E. W., Böhm, K. H., & Mannery, E. 1981, ApJS 47, 117
Calvet, N., Cantó, J., Binette, L., & Raga, A. C. 1992, RevMexAA, 24, 81
Choe, S. U., Böhm, K. H., & Solf, J. 1985, ApJ, 288, 338
Eislöffel, J., Mundt, R., & Böhm, K. H. 1994, AJ, 108, 1042
Girart, J. M., Viti, S., Williams, D. A., Estalella, R., & Ho, P. T. P. 2002, A&A, 388, 1004
Haro, G. 1952, ApJ, 115, 572
Hartigan, P., Raymond, J. C., & Hartmann, L. W. 1987, ApJ, 316, 323
Hartmann, L. W., & Raymond, J. C. 1984, ApJ, 276, 560
Henney, W. J. 1994, ApJ, 427, 288
________. 1996, RevMexAA, 32, 3
Henney, W. J., & Axon, D. J. 1995, ApJ, 454, 233
Henney, W. J., Raga, A. C., & Axon, D. J. 1994, ApJ, 427, 305
Herbig, G. H. 1951, ApJ, 113, 697
________. 1973, IBVS, 832, 1
Herbig, G. H., & Jones, B. F. 1981, AJ, 86, 1232
Hester, J. J., Stapelfeldt, K. R., & Scowen, P. A. 1998, ApJ, 116, 372
Laval. A., Boulesteix, J., Georgelin, Y. P., Georgelin, Y. M., & Marcelin, M. 1987, A&A, 175, 199
Noriega-Crespo, A., Calvet, N., & Böhm, K. H. 1991, ApJ, 379, 676
Noriega-Crespo, A., Garnavich, P. M., Curiel, S., Raga, A. C., & Ayala, S. 1997, ApJ, 486, L55
Pravdo, S. H., Rodríguez, L. F., Curiel, S., Cantó, J., Torrelles, J. M., Becker, R. H., & Sellgren, K. 1985, ApJ, 293, L35
Pravdo, S. H., Feigelson, E. D., Garmire, G., Maeda, Y., Tsuboi, Y., & Bally, J. 2001, Nature, 413, 708
Raga, A. C., Barnes, P. J., & Mateo, M. 1990, AJ, 99, 1912
Raga, A. C., & Böhm, K. H. 1985, ApJS, 58, 201
________. 1987, ApJ, 323, 193
Raga, A. C., Mateo, M., Böhm, K. H., & Solf, J. 1988, AJ, 95, 1783
Raymond, J. C., Hartmann, L. W., & Hartigan, P. 1988, ApJ, 326, 323
Reipurth, B., Heathcote, S., Yu, K. C., Bally, J., Rodríguez, L. F. 2000, ApJ, 534, 317
Rodríguez, L. F., Delgado-Arellano, V. G., Gómez, Y., et al. 2000, AJ, 119, 882
Schwartz, R. D., Cohen, M., Jones, B. F., et al. 1993, AJ, 106, 740
Solf, J., Böhm, K. H., & Raga, A. C. 1988, ApJ, 334, 229
Solf, J., Raga, A. C., Böhm, K. H., & Noriega-Crespo, A. 1991, AJ, 102, 1147
Strom, S. E., Strom, K. M. Grasdalen, G. L., et al. 1985, AJ, 90, 2281
Torrelles, J. M., Rodríguez, L. F., Cantó, J., Anglada, G., Gómez, J. F., Curiel, S., & Ho, P. T. P. 1992, ApJ, 396, 95

Philippe Amram and Jacques Boulesteix: Laboratoire d'Astrophysique de Marseille, 2 Place Le Verrier, 13248 Marseille, France (Philippe.Amram@oamp.fr, jacques.boulesteix@oamp.fr).
Alejandro C. Raga: Instituto de Ciencias Nucleares, UNAM, Apdo. Postal 70-543, 04510 México, D. F., México (raga@nucleares.unam.mx).
Bo Reipurth: Institute for Astronomy, University of Hawaii, 640 N. Aohoku Place, Hilo, HI 96720, USA (reipurth@ifa.hawaii.edu).
Angels Riera: Departament de Física i Enginyeria Nuclear, Universitat Politècnica de Catalunya, Av. Víctor Balaguer s/n, E-08800 Vilanova i la Geltrú, Spain (angels.riera@upc.edu).
Oswaldo Toledano: Instituto de Astronomía, UNAM, Apdo. Postal 70-264, 04510 México, D. F., México.